

www.acsami.org Research Article

Stress Bearing Mechanism of Reduced Graphene Oxide in Silicon-Based Composite Anodes for Lithium Ion Batteries

Mahmud Tokur,* Mok Yun Jin, Brian W. Sheldon, and Hatem Akbulut



Cite This: ACS Appl. Mater. Interfaces 2020, 12, 33855-33869



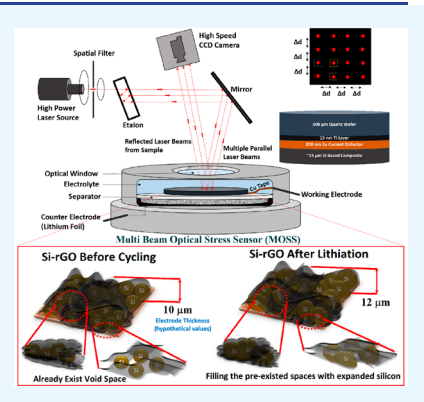
ACCESS

Metrics & More



Supporting Information

ABSTRACT: Despite the significant research that has been carried out to improve cycling performance of lithium ion batteries (LIB) with silicon (Si) based composite electrodes, limited studies have been performed on these materials to evaluate the effects of internal microstructural changes and stress evolution on the electrochemical performance. Here, combined ex situ and in situ investigations on the accommodation of volume expansion in Si-based nanocomposite electrodes are reported. This work emphasizes the importance of conductive agents in light of the poor electronic conductivity of Si. A detailed comparison between commonly used carbon black (CB) and reduced graphene oxide (rGO) shows that these materials have substantial effects on microstructural evolution and internal stress in Si based composite electrodes that are employed in lithium ion cells. This study provides the first monitoring of stress evolution in Si-rGO based composite electrode during electrochemical cycling using in situ wafer curvature measurements. The prepared Si-rGO based electrode exhibits almost 10 times lower stress generation and consequently higher



cycling performance in electrochemical cells. The resulting 3D networked structure not only acts as an electronic conduit to the encapsulated active materials but also serves as a mini-electrochemical reaction chamber which hinders the formation of the solid electrolyte interphase (SEI) and limits the pulverization of active material and the evolution of severe stress during cycling. Moreover, investigations of the microstructural changes and internal charge transfer resistance in the electrodes after cycling provide further evidence that rGO produces superior structures for energy storage.

KEYWORDS: lithium ion battery, silicon anode, reduced graphene oxide, in situ stress analysis, multibeam optical stress sensor

■ INTRODUCTION

Rechargeable lithium ion batteries at present play an important role in the life quality of modern society as the dominant technology using in power supplies for portable electronics and electric vehicles. 1-3 However, the energy density of current state-of-the-art LIBs have still less than 300 Wh/kg due to the limited specific capacity of currently used electrode materials.⁴ Therefore, the development of LIBs with a reduced weight, higher capacity, and longer life spans is urgently desired.5 Conventional carbonaceous anode materials such as graphite offer just a 372 mAh/g theoretical capacity through intercalation reaction.6 This is an important bottleneck in lower energy density, and it cannot satisfy the demand for high capacity in LIBs but still remains the primary choice owing to the low cost and high electronic conductivity. Among wellstudied anode materials, Si has been identified as one of the most promising alternatives for next generation LIBs with the highest theoretical specific capacity, natural abundance, ecofriendliness, and competitive costs. The maximum capacity for most applications is 3579 mAh/g, which is almost 10 times higher than that of graphite (capacity up to 4200 mAh/g can also be achieved at a higher temperatures).^{8,9} Unfortunately, the implementation of Si anodes has suffered from its poor electrical conductivity and large undesirable volume changes (>300%) during electrochemical reactions. 9,10 This causes substantial mechanical degradation during repeated expansion and contraction of the electrode and loss of contact between the active material and the current collector. 11,12 Moreover. mechanical stress due to the repeated volume change leads to cracking in the SEI layer which forms on the surface of Si, due to decomposition of the organic electrolyte. 9,13 The issues of electronic isolation of particles, loss of mechanical integrity of composite electrode and interfacial instability results in impedance rise, rapid capacity fade, and deteriorated battery performance. 14,15 Recent efforts have been taken to overcome conductivity issue of intermetallic-based active materials by supported them with conductive materials (e.g., carbon, metal, and conductive polymers). ¹⁶⁻²⁰ Carbonaceous materials, such as amorphous carbon (AC), ²¹⁻²³ conductive carbon black (CB),²⁴ carbon nanotube (CNT),²⁵ and graphene (rGO), 26-28 are widely used in lithium ion cells to enhance

Received: June 2, 2020 Accepted: July 6, 2020 Published: July 6, 2020





the electrical conductivity of electrodes. 16,29 However, with conventional additives like CB the surfaces of active materials are still directly exposed to the electrolyte, leading to the formation of unstable SEI and severe pulverization. To alleviate electrode failure from volumetric change-induced mechanical cracking and dead particle generation, a combination of Si with rGO has been proposed.30 The strong and flexible 3D network of rGO not only assists the charge transfer but also buffers the volume change, protects the mechanical integrity, reduces the internal stress, and acts as a blocking layer of electrolyte to control the SEI formation on the surface The common studies have focused on preparation methods and electrochemical properties of electrode materials used in LIBs. In the past few years, new experimental techniques and methods have also been developed for measurements of structural deformation, internal conditions, and stress responses.35-

This study focuses on the microstructural changes and stress evolutions of Si-based composite anodes during insertion/ extraction with the understanding that stresses drive mechanical failure and damage in lithium ion cell. In situ and ex situ analyses have been carried out to understand the relationship between conductive agents and active materials during electrochemical reactions. To this end, we have built a multibeam optical stress sensor (MOSS) system with a special electrochemical cell and carried out real-time stress measurements on rGO-based electrode for the first time in this study. Additionally, we correlate these stresses to electrochemical, structural, and phase evolution via combined scanning electron microscopy, transmission electron microscopy, focused ion beam, and X-ray diffraction. It is revealed that the lithiationinduced stresses strongly depend on the internal design of conductive agents and active materials. These results may provide important insight into the fully coupled stress generation and internal change in Si-based composite anodes of LIBs.

■ EXPERIMENTAL SECTION

Preparation of Si-rGO Composite. The Si-rGO composite was prepared by mixing graphene oxide (GO) solution and silicon (Si, ~100 nm in size, 98% purity, Sigma-Aldrich) nanoparticles followed by the reduction process. Graphite oxide was used as a starting material, which is obtained with modified Hummers' method, 42 to fabricate the reduced graphene oxide encapsulated in silicon composite due to its hydrophilic affinity and homogeneous dispersion capability in an aqueous solution. In a typical process, GO suspension was obtained by exfoliation of graphite oxide in nanopure water. Before immersing Si nanoparticles into this solution, the surface of the Si structures was charged positively with 3-aminopropyl-trimethoxysilane (APTES, Sigma-Aldrich) in toluene (Sigma-Aldrich) (95:5 volume %) for 24 h. GO nanolayers consist of covalently attached oxygen-containing groups, such as hydroxyl, epoxyl, carbonyl, and carboxyl groups which means it is naturally negatively charged.⁴ Next, the mixture was sonicated in an ultrasonic bath for 5 h and stirred for 12 h which provides a good decoration of 70 wt % aminemodified (positively charged) Si nanoparticles into 30 wt % naturally negatively charged GO nanolayers. The main reason for choosing 7:3 ratio for Si and GO is based on a Karl Fischer analysis by Stankovich et al. which is detailed in our previous study.44 Shortly, the hygroscopic nature of GO contains a higher oxygen level (-25% water) than that of the hydrophobic nature of rGO. In other words, most of the oxygen in GO is removed from the system after a successful reduction process that results in mass loss of about 20 wt %.43 It was assumed that the 3:7 ratio will change to about 1:3 after reduction of GO which is very important to prepare the desired

electrode combination. These estimates were proven and described with thermal analysis. The reduction was carried out by adding hydroiodic acid solution (HI, 57%, Sigma-Aldrich) into the Si-GO mixture in a sealed cuvette that was placed in a thermostated water bath at 80 °C for 2 h. Pei, Songfeng et al. have compared the effect of different reducing agents (HI reduction, NaBH4 reduction, and hydrazine reduction) on the properties of GO film.⁴⁴ They have suggested that HI acid reduction can achieve highly conductive and flexible rGO films. Moreover, they have also reported that this reduction method maintains good integrity and even improves the strength and ductility of the original GO films.⁴⁵ The final product was centrifuged and washed several times with ethanol and nanopure water. Because of agglomeration and stacking issues at high temperatures, the centrifuged composite was freeze-dried to obtain better structure (high surface area and good flexibility of rGO) for the next steps.

Preparation of Composite Electrodes. In order to show the advantages of rGO on the Si-based composite anodes, Super P carbon black (CB, Timcal) and rGO were used as reinforcing elements separately under the same conditions. Silicon nanoparticles were used as active materials and carboxymethyl cellulose (CMC, Sigma-Aldrich) was used as a binder in obtained composites. Electrodes were classically prepared with the following formulation: 60 wt % Si as the active material, 20 wt % CB or rGO as the conductive agent and 20 wt % CMC as the binder. To prepare the homogeneous slurry, the CMC binder was first dissolved in nanopure water with 4 wt % concentration and then selected amount of powders were dry mixed mechanically in an agate mortar. The as-synthesized Si-rGO composite powders were used to obtain Si-rGO-CMC nanocomposite electrode. Finally, the binder solution was added and mixed for an additional 30 min. The obtained slurry was then casted onto a 25 μ m thick copper foil and coated using a doctor blade. After leaving it for 1 h in ambient atmosphere, the drying process was carried out in a vacuum oven at 70 °C for 10 h to remove the remaining solvent. The total mass of electrodes is calculated about 1.5 mg (0.9 mg Si, 0.3 mg carbon, 0.3 mg binder).

In Situ Stress Measurements. Preparation of working electrodes for in situ stress measurements are different from conventional button cell electrodes. Five hundred micrometers of quartz glass wafers were used as the substrate. Fifteen nanometers of Ti as a bonding layer and 200 nm of Cu as a current collector were deposited by E-beam. Film thicknesses were controlled during the process. The 15 nm Ti layer improves adhesion between the quartz and the Cu current collector and provide homogeneous stress distribution through the electrode (poor adhesion is observed when the Cu film is deposited directly on the quartz substrates).46 A basic principle of this measurement is monitoring the curvature change of the elastic substrate (quartz wafer) by a multibeam optical sensor (MOS) wafer-curvature system (k-Space Associates, Dexter, MI). Laser beams are focused on the backside of the quartz substrate. The stiff substrate constrains expansions and contractions in the in-plane dimensions of the active thin film (here Si-rGO composite) during lithiation/delithiation. This leads to bending of the substrate/thin film system, which deflects the laser beams as they are reflected back from the substrate. By monitoring the changes in the spot spacing of the deflected beams that are reflected from the backside of a substrate, stress development in the film can be measured in real time (in situ). Since the quartz substrate deforms elastically, the stress in the active film(s) is proportional to the induced change in wafer curvature, which can be determined quantitatively with established relationships.

Material Characterization. Structural characterization of composite electrodes before and after electrochemical cycling, were characterized using high-resolution X-ray diffraction (XRD, Bruker D8 Discovery) with 2θ range from 5° to 80°. Surface morphologies of the as-prepared and as-cycled films were examined by field-emission scanning electron microscopy (FESEM, FEI, HELIOS 600) and transmission electron microscope TEM (FEI, CM 20). Focused ion-beam (FIB) was used to obtain cross-sectional views of the electrodes and to determine the film thicknesses. Elemental MAP and line analysis of the composite films were carried out to understand

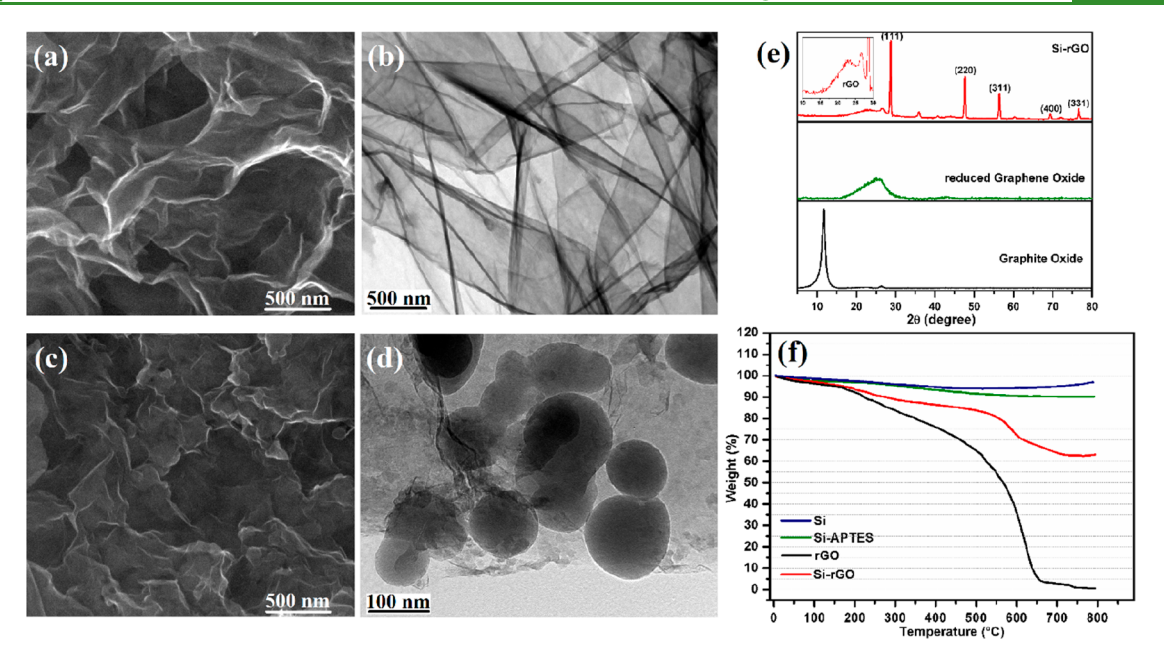


Figure 1. SEM and TEM images of (a,b) rGO and (c,d) Si-rGO composite. (e) XRD analysis of graphite oxide, reduced graphene oxide, and Si-rGO composite. (f) TGA curves of Si, Si-APTES, rGO, and Si-rGO composite.

elemental composition and homogeneous distribution of nanostructured materials. The weight ratio of total carbon content in the final Si-rGO composite powder was evaluated by thermal gravimetric analysis (TGA, SDT Q600, TA Instrument). The sample was heated up to 800 $^{\circ}\text{C}$ at a ramping rate of 10 $^{\circ}\text{C/min}$, and the test was conducted in dry air atmosphere.

Electrochemical Measurements. The electrochemical tests of composite electrodes were performed in coin-type CR2032 test cells assembled in an Ar-filled glovebox. As-prepared composite electrode was used as the working electrode while pure lithium metal foil was used as the counter electrode in the lithium ion cell. The two electrodes were separated by a Celgard separator. One molar LiPF₆ was dissolved in a mixture of ethylene carbonate (EC) and diethyl carbonate (DEC) (EC/DEC 1:2 wt.). A standard liquid electrolyte was used with fluoroethylene carbonate (FEC, 10% wt.) additive. Electrochemical tests of composite electrodes were controlled with a Bio-Logic VMP3 potentiostat, employing a cutoff voltage range from 0.05 to 1.5 V at room temperature.

■ RESULTS AND DISCUSSIONS

Structure of rGO Based Electrodes. The complete fabrication of the Si-rGO nanocomposites includes two selfassembly processes: (i) the Si nanoparticles were first modified with APTES to change the surface charge from negative to positive; and (ii) the amine-functionalized Si nanoparticles were hybrid assembled with negatively charged GO by electrostatic attraction. Zeta potential measurements were used to survey the assembly process. The zeta potentials of Si particles changed from -21 mV to +58 mV after charging with APTES. The natural zeta value of GO solution was measured as -66 mV. This method facilitates good dispersion of the Si nanoparticles between GO nanolayers. The electrostatic repulsion between the positively charged nanoparticles prevents the formation Si particle agglomerates (confirmed by the optical images of the pure Si-GO mixture and positively charged Si-GO mixture in Figure S1). This method facilitates good dispersion of the Si nanoparticles between GO nanolayers, leading to a well-dispersed composite structure. Milky brown solution in pure Si-GO mixture represents the Si distribution of nanopure water. Stacked and undecorated GO

clumps are also shown in the solution. The well-decorated and modified Si can easily be discriminated with naked eyes. Color change is not observed between seaweed-like GO in clear solution and that means all the modified Si nanoparticles are wrapped by negative charged nanolayers. Because of excellent mechanical and electrochemical properties of rGO, this well-dispersed composite structure provides a "flexible confinement function" for tolerating volume changes. Moreover, homogeneous distribution of this multicomponent composition allows integrated conductive network and plenty of channels, which result in increased reaction of the Si nanoparticles with lithium ions and greatly improved the electrical conductivity of the entire electrode in lithium ion cells.

Open porous structure of rGO was analyzed with SEM and TEM. The images in Figure 1a,b show that the stacking problem was not observed thanks to HI reduction. This method maintains the integrity and flexibility of the layered and wavy surface morphology without destroying thanks to the nucleophilic substitution reaction.⁴⁵ The images of the Si-rGO nanocomposite in Figure 1c,d indicate that nanovoids in the rGO layers were filled with Si nanoparticles. The electrostatic interaction between positively charged Si and negatively charged GO promotes this wrapping and also promotes adhesion between the Si and rGO. In other words, negative GO layers wrapped all the positive Si nanoparticles then reduced them with HI acid. The oxygen functional groups in the GO structure (such as hydroxyl, epoxyl, carbonyl, and carboxyl groups) were capable of anchoring Si nanoparticles. The amine group (-NH₂) on the surface of Si nanoparticles acts as a bridge connection between Si and GO (C) to form the Si-NH-C(O)- structure. This finding is also an indication of good adhesion between Si and rGO. The hybrid architecture was further confirmed with TEM images. The distribution of Si nanoparticles with a diameter of ~100 nm in an rGO matrix are shown in Figure 1d. The folds in the spongy rGO structure indicate that this consists of relatively homogeneous, unagglomerated, and thin nanolayers. This composite structure is designed to curtail mechanical stresses

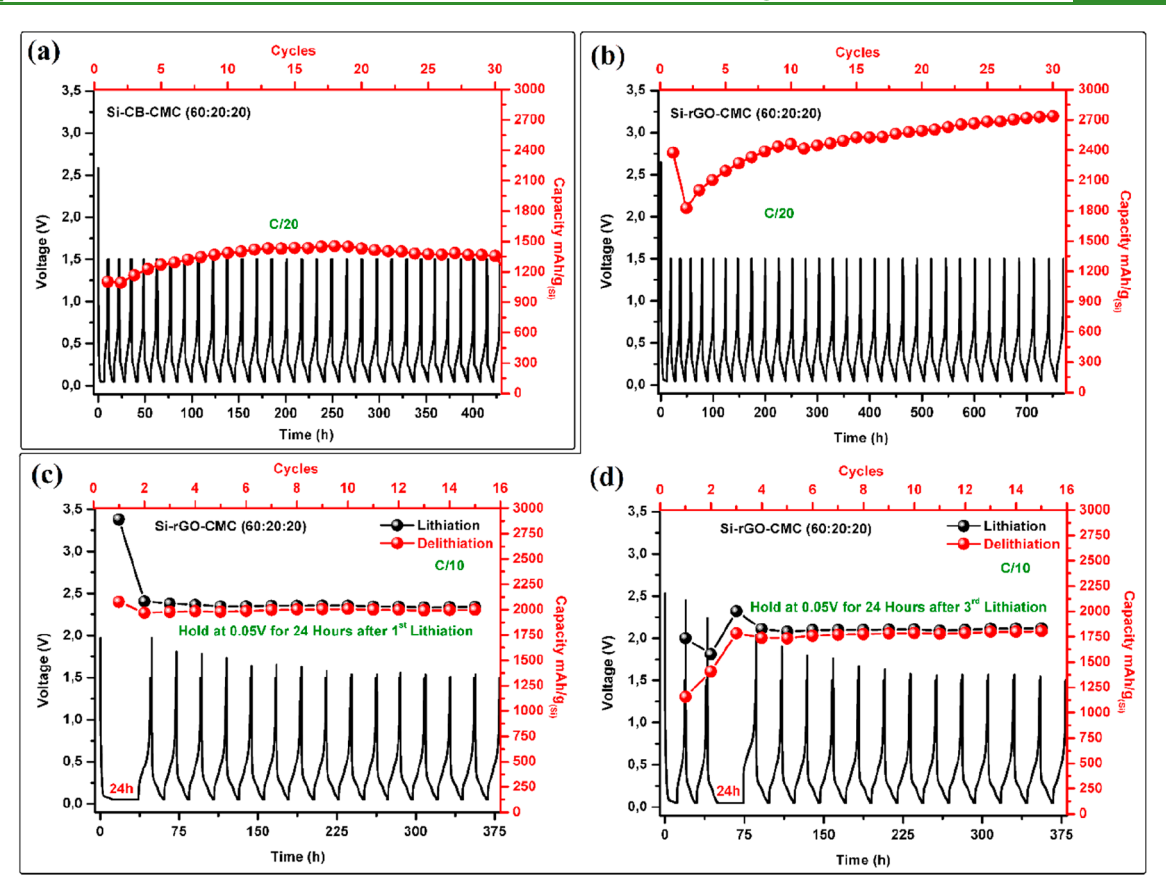


Figure 2. Cycling results (cycled with C/20) and time-voltage curves of Si-CB-CMC (a) and Si-rGO-CMC (b) electrodes. Additional protocols were also used for the Si-rGO-CMC electrodes: (c) 24 h hold after first discharge and (d) 24 h hold after third discharge.

with sufficient void space for Si volume expansion and contraction during electrochemical cycling. Experimental results which demonstrate this are presented below and discussed further in subsequent sections.

X-ray diffraction patterns of graphite oxide (starting material), reduced graphene oxide, and Si-rGO are shown in Figure 1e. The diffraction peak for graphite flakes ($\sim 26^{\circ}$) has completely disappeared after the oxidation process with a new peak at 11.76° which confirms the conversion to graphite oxide (oxygen was bonded to planar surface of carbon structure results in shifting the diffraction peak).⁴² After the reduction process of graphite oxide dispersion (graphene oxide), the diffraction peak around 2θ values of 11.76° has completely disappeared and a new broad peak emerged between 18.24° and 28.04° which indicates that GO has been reduced to rGO successfully. In the self-assembled preparation process used in this study, the Si-GO solution was obtained by exfoliation of graphite oxide in nanopure water followed by mixing with modified Si nanoparticles. Reduction of GO was then carried out in the same aqueous solution. HI acid not only reduces the GO but also removes the native oxide layer on the surface of Si nanoparticles, and thus improves the electrochemical properties of the composite electrodes. After this step, Si nanoparticles between nanolayers were protected from ambient because of the hydrophobic nature of rGO. After the electrode preparation process, the new weak broad peak between 18.24° and 28.04° also emerged, which corresponds to the rGO in the Si-rGO composite (Figure 1e). The absence of the graphite oxide peak at 11.76° indicates that the GO was also successfully reduced to rGO in the composite system, and

the characteristic Si peaks (28.74°, 47.6°, and so forth) indicate that the nanoparticles are crystalline.

The layer number of reduced graphene oxide was calculated by the Debye–Scherrer method

$$La = \frac{0.89\lambda}{\beta \cos \theta} \tag{1}$$

$$\eta = \frac{\text{La}}{d} \tag{2}$$

where La (stacking height), β (full width half maximum (fwhm)), η (number of reduced graphene oxide layers), and d (interlayer spacing) were obtained by using the data from XRD patterns. On the basis of these equations, the reduced graphene oxide consists of 12 layers with an estimated thickness of 4.3 nm. This small number of layers is possible because the homogeneously intercalated Si nanoparticles in the GO layers prevent the rGO sheets from restacking. This facilitates the electrolyte diffusion and further enhances the Li ions intercalation to improve its electrochemical performance. In addition, freeze-drying is also an effective factor to avoid a restacking problem due to the low-temperature process.

Quantitative composition analysis of the Si-rGO composites obtained by TGA under dry air atmosphere measurements of Si, Si-APTES, rGO, and Si-rGO was performed separately to determine the Si and rGO content and to understand the decomposition mechanisms. As shown in Figure 1f, weight losses of $\sim\!\!5\%$ occur between 30 and 200 °C for all samples, due to the removal of adsorbed water. The weight losses between 200 and 750 °C for the rGO-containing samples

indicate the oxidation and decomposition of rGO in air. Small weight increases after 600 $^{\circ}\text{C}$ are probably due to limited Si oxidation. There is also a 5% weight loss difference between modified and unmodified Si due to decomposition of organic $-\text{NH}_2$ compounds between 350 and 800 $^{\circ}\text{C}$. The TGA results shown here indicate that the weight ratio of the Si/rGO in the composite system is approximately 3:1 based. These materials were used to create the desired Si–rGO–CMC (60:20:20) composite electrodes.

Electrochemical Cycling. The rGO derived electrodes were directly compared with CB particle-based electrodes with the same approximate silicon carbon content and the same CMC binder loading. The cycle performances were evaluated with galvanostatic charge-discharge tests at slow and medium rates (C/20, C/10, and C/2) between 0.05 and 1.5 V, displayed in Figure 2a,b. Specific discharge capacities were calculated based on only the Si loading (i.e., the CB contribution was assumed to be negligible). The open circuit potential (OCV) of both types of electrodes is approximately 2.6 V versus Li⁺/Li. The initial capacities of CB- and rGObased electrodes are 1104 and 2374 mAhg⁻¹, respectively. In Figure 2a, the discharge capacity of the CB-containing electrode increases slightly until the 20th cycle, where it reaches a maximum value of 1454 mAhg⁻¹. Therefore, the volume change of Si cannot be accommodated effectively, and the conductive network cannot disperse well in the electrode upon cycling. First cycle irreversible capacity loss is not observed for the CB-based electrode and is probably due to a high amount of CMC binder (20%). The surface areas of composite electrodes are much higher than commercial electrodes because of using nanometer-sized active particles. That is why relatively high binder content was selected in this

In contrast, the discharge capacity of rGO-containing electrodes generally decreases after the first cycle to 1825 $mAhg^{-1}$ (-23%) for the results in Figure 2b. The capacity then increases progressively to 2738 mAhg⁻¹ (+15%) in the 30th cycle here. The capacity increase in the initial cycles has been attributed to gradual activation of Si nanoparticles between the rGO layers and side reaction from electrolyte (i.e., due to the formation of SEI). Indeed, similar results have been reported in many previous studies of Si-based electrodes. 49,50 CV analysis of rGO-based electrode, given in Figure S2, also supports the gradual activation of Si nanoparticles inside the continuous carbon framework. The initial 10 cycles of the electrode are carried out in a potential window of 0.05-1.5 V at a scan rate of 0.05 mV/s. During the lithiation stage of the CV test, a broad peak, which ascribes with the SEI formation, can easily be seen between ~1 and ~0.2 V in the first cycle and it disappears in the subsequent cycles. The main peaks of the alloying reaction of crystalline Si to lithiated amorphous Si (Li_xSi) in lithium ion cell are located at about 0.2 V. These peaks are aroused after the first scanning cycle and the peak current density and integrated area intensity are evolved gradually, indicating a gradual activation of Si. As the discharge capacity of rGO-containing electrode was unstable (positively) during the cycling, in this study it was hypothesized that the capacity variations were primarily caused by internal structural changes. This includes changes both inside and between the SirGO bundles. For example, the Si nanoparticles that are wrapped with rGO are believed to be strongly bonded to the carbon nanolayers, which allows integrated conductive network, as explained before. The large volumetric Si expansion

leads to expansion of the rGO layers during first lithiation. During delithiation, contraction of lithiated Si creates some voids between active material and conductive agent which result in decrement of lithiation reactions due to partial contact loss. While this phenomenon may cause a relative capacity fading for initial cycles, it also provides the protection of reversible stress in lithium ion cell over long cycles. To investigate this effect, different formation protocols were applied on the Si-rGO-CMC electrode such as 24 h hold after the first lithiation and 24 h hold after the third lithiation. Electrodes were cycled with C/10 to make a quick comparison. In the Figure 2c, lithium ion cell prepared with Si-rGO-CMC was lithiated to 0.05 V in 10 h and was held at this voltage for an additional 24 h. Since the current value displayed a very low amount after 24 h, the delithiation process was started with a standard protocol then tested for 15 cycles. In Figure 2d, another Si-rGO-CMC electrode was prepared and tested for three cycles. The same formation protocol was applied after the third lithiation at this time and tested until the 15th cycle. As a result of this observation, it was understood that quite reproducible profiles upon both discharge and charge are evidenced after a deep lithiation process. Note that the difference on capacity between two electrodes in Figure 2c,d depends on mass loading. While the total mass of the electrode in Figure 2c is calculated at 1.4 mg, the electrode in Figure 2d is measured at 2.7 mg. It is also known that the specific capacity of the high mass loading electrodes (thicker) are slightly lower than that of the low mass loading electrodes (thinner), depending on Li+ ion flow process throughout whole electrode. If not mentioned, the capacities of electrodes in Figure 2c,d are lower than that of the electrode in Figure 2b (even though it was prepared with same combinations) due to a carried out different C rate. High C rate usually leads to low capacity in lithium ion cells. Also, another positive attribute of all of the reported results related with rGO is high Coulombic efficiency after the first cycle (whether or not the formation has been applied). In order to compare the electrochemical cycling behavior of both electrodes (CB and rGO containing) in the case of the same formation protocols, charge-discharge tests were carried out with C/2 current rate for 85 cycles as shown in Figure S3. It is shown that the Coulombic efficiencies of the electrodes are fairly stable at about 100%. However, the specific capacities are relatively low as expected at higher current rate. Initial capacities of the electrodes are rather close to each other both in lithiation and delithiation cases. The big difference is started after the first cycle in the cell consisting of CB. While the rGO reinforced electrode shows the similar behavior as presented before, specific capacity of the CB reinforced electrode is decreased continuously. It is most likely due to the strong lithiation reaction of Si particles and the repetitive formation of SEI (due to volume changes) that cannot control conductive material and destroyed the electrode structure, resulting in electrochemical failure in the subsequent cycles. SEM images of these electrodes analyzed after the first lithiation are given in Figure S4 to investigate this effect in particle size. Huge volume expansion of Si particles can be easily observed in the CB-based electrode. Note that no formation is applied to the electrodes. Because of that the activation of Si particles is not completed in the rGO-based electrode and the volume expansion displayed was very limited in the figure. In order to compare the effects of binder and carbonaceous additives on the electrochemical performance of lithium ion cells, charge-discharge tests of the composite

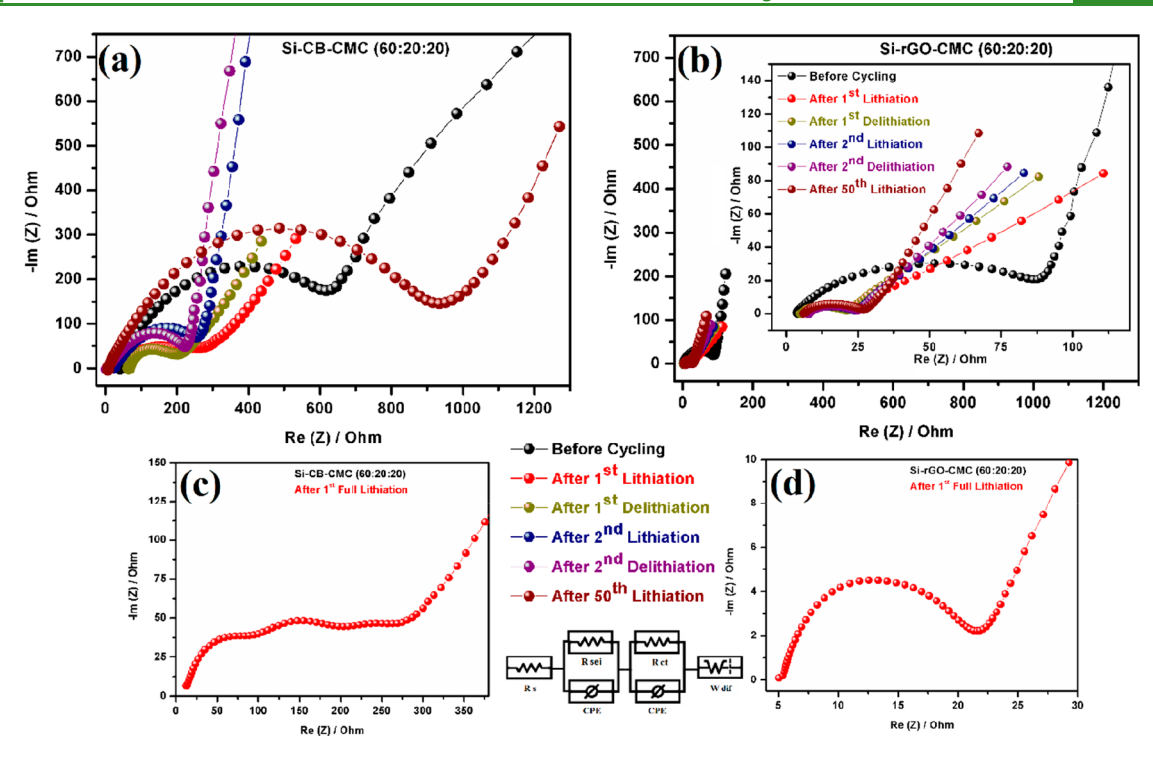


Figure 3. Impedance analysis of Si–CB–CMC (a) and Si–rGO–CMC (b) composite electrodes before and after some cycles. To better understand the SEI-related impedance changes, EIS curves of Si–CB–CMC (c) and Si–rGO–CMC (d) composite electrodes (after first lithiation) were displayed with higher magnification.

electrodes were also performed with 80:10:10 combinations. The results in Figure S4 show that discharge capacities and electrochemical stabilities of these electrodes are much lower than the 60:20:20 combinations. With the increased silicon levels in the electrodes, the surface area for SEI formation and the internal electrode structure apparently degrades faster. Thus, we used higher amounts of binder and carbon-based conductive agent in the electrodes for this study.

In situ electrochemical impedance spectroscopy (EIS) analysis of the composite electrodes is presented in Figure 3 to investigate the internal resistances before cycling and after the first lithiation, first delithiation, second lithiation, and second delithiation. EIS analysis of electrodes is also examined after the 50th lithiation to show the contribution of rGO. The results were analyzed with an equivalent circuit model, which includes electrolyte resistance (R_S) , SEI resistance (R_{SEI}) , charge transfer resistance (R_{CT}) , and a Warburg diffusion element (W_{DIF}) , respectively. Most of the spectra show an approximate semicircle that reflects the combined effects of SEI resistance and charge transfer resistance as well as the double-layer capacitance at the electrode/electrolyte interface. In low frequency, the Warburg contributions are associated with diffusion. To make an easy comparison, the charge transfer resistance of electrodes are shown in Figure 3a,b. The fitted parameters of the EIS analysis of composite electrodes are also listed in Table 1. Nyquist plots of the composite electrodes in half-cells show that the rGO-based electrode exhibits significantly higher conductivity. Before electrochemical cycling, the combined interface impedance value shown here is much higher in the CB-containing electrode (~870 Ω) than in the rGO-containing electrode (~115 Ω). Charge-transfer resistances of both electrodes were significantly reduced after first lithiation and did observe a significant increase for two cycles. This result is commonly seen in Si-

Table 1. Fitted Resistance Values in the Equivalent Circuit

electrodes	cycling status	$R_{\rm S} \; (\Omega)$	$R_{\mathrm{SEI}}\left(\Omega\right)$	$R_{\mathrm{CT}}\left(\Omega\right)$
Si-CB-CMC	before cycling	40.70	2.12	868.82
(60:20:20)	after first lithiation	2.35	190.40	360.75
	after first delithiation	63.70	6.36	280.19
	after second lithiation	22.68	21.20	370.87
	after second delithiation	3.80	5.44	300.31
	after 50th lithiation	7.50	29.81	1110.23
Si-rGO-CMC	before cycling	1.60	1.77	116.90
(60:20:20)	after first lithiation	0.39	4.60	26.46
	after first delithiation	2.65	2.45	21.10
	after second lithiation	6.17	2.50	29.67
	after second delithiation	6.80	2.61	28.31
	after 50th lithiation	1.61	4.43	32.78

based electrodes. The interfacial resistance of the CB-containing electrodes was also greatly increased after 50th cycles. It is most likely due to continuous SEI formation and contact loss between the active material and current collector that was generated with volume change and stress evolution in the electrode. In contrast, there is a much smaller increase in the interfacial impedance in the rGO-containing electrodes after the 50th cycle. This could be ascribed to protection of Si nanoparticles inside of the turbostratic packed rGO layers, which prevent delamination and electrical isolation of the electrode after prolonged cycles. Detailed comparison was carried out in Figure 3c,d with higher magnification of Nyquist curves obtained after the first lithiation. As expected, charge-transfer resistance of the rGO-containing electrode was much

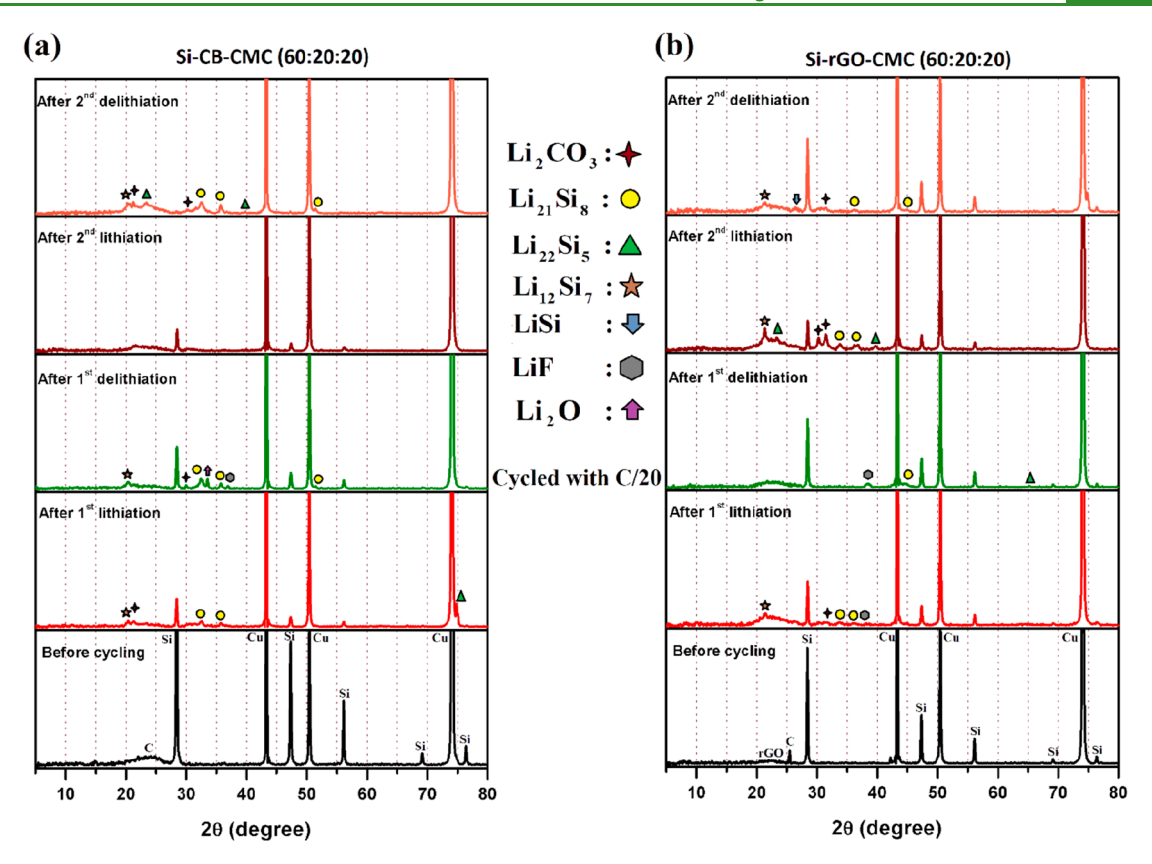


Figure 4. XRD results of as-prepared and as-cycled composite electrodes for (a) Si-CB-CMC and (b) Si-rGO-CMC. (Scanning was carried out on a composite film coated on Cu foil.)

lower than that of the CB-containing electrode. In addition, three different semicircles were observed in Figure 3c, while only one semicircle was seen in Figure 3d. This can be explained by the following: (1) excessive SEI formation leads to the development of a second semicircle and (2) large cracks on the composite electrode and peeling between current collector and active materials (described later) results in the occurrence of a third semicircle in the CB-containing electrode. As an indicator of these possible approximations, the SEI resistance of the CB-containing electrode after the first lithiation is much higher than that of the rGO-containing electrode.

X-ray diffraction patterns of composite electrodes before cycling and after first lithiation, first delithiation, second lithiation, and second delithiation are reported in Figure 4. The reason for Cu peak existence is Cu foil. The results for both composite electrodes are very similar before electrochemical cycling with the peaks for crystalline Si and disordered graphitic C. Some variations in the peak intensities were related to the coexistence of crystalline and amorphous Li_xSi_y phases, labeled in the Figure 4, during Li⁺ insertion and extraction process. The decrease of the main peak intensity with increasing Li in Li_xSi_y is thus a characteristic trend of the Li–Si alloys.

The patterns of as-cycled electrodes corresponded well with $\rm Li_2CO_3$ (#72-1216), LiF (#04-0857), and Li₂O (#12-0254) (related with SEI) and $\rm Li_{22}Si_5$ (#73-2049), Li₂₁Si₈ (#33-0817), Li₁₂Si₇ (#41-1308), and LiSi (#72-6652) (related with lithiated Si). S1-SS The most important difference in these results is that the Si peaks are no longer present for the CB-containing composite electrode after the second delithiation. This

indicates that the Si nanoparticles were fully activated. In contrast, activation of the Si nanoparticles continues to occur in the rGO-containing electrode. These results are in good consistency with the cycling tests and EIS analysis. Estimated Si particle sizes were also obtained with the Debye—Scherrer's equations. About one hundred nanometers of commercial Si nanoparticles was used for all experiments. This is also confirmed with SEM, TEM, and XRD analysis. After the first lithiation, the average particle sizes in the CB-containing electrode and rGO-containing electrodes are ~360 nm and ~140 nm, respectively. After delithialion, the particle sizes decreased to ~210 nm (for CB-containing) and ~105 nm (for rGO-containing).

Stress Evolution. Stress generation and evolution of SirGO-CMC (60:20:20) electrode was measured with MOSS system using a custom-built electrochemical cell modeled in Figure 5a. Compressive stress of the electrode was analyzed based on capacity of the cell. To do this, galvanostatic and MOSS systems were combined together and operated simultaneously. Electrochemical experiments are conducted at C/20 rate to investigate the stress generations. An elastic substrate was used in a specially designed electrochemical cell which prevents the in-plane expansion of the composite film, resulting in compressive stress in the film, and it increases with the time (or capacity) upon lithiation. Digital images of the preparation steps of the MOSS electrodes are given in Figure S5.

A concomitant evolution of nominal stress and cumulative capacity for Si-rGO-CMC composite electrode in three cycles is presented in Figure 5b. Initial lithiation capacity of the cell was 2640 mAhg⁻¹, while nominal stress in the electrode

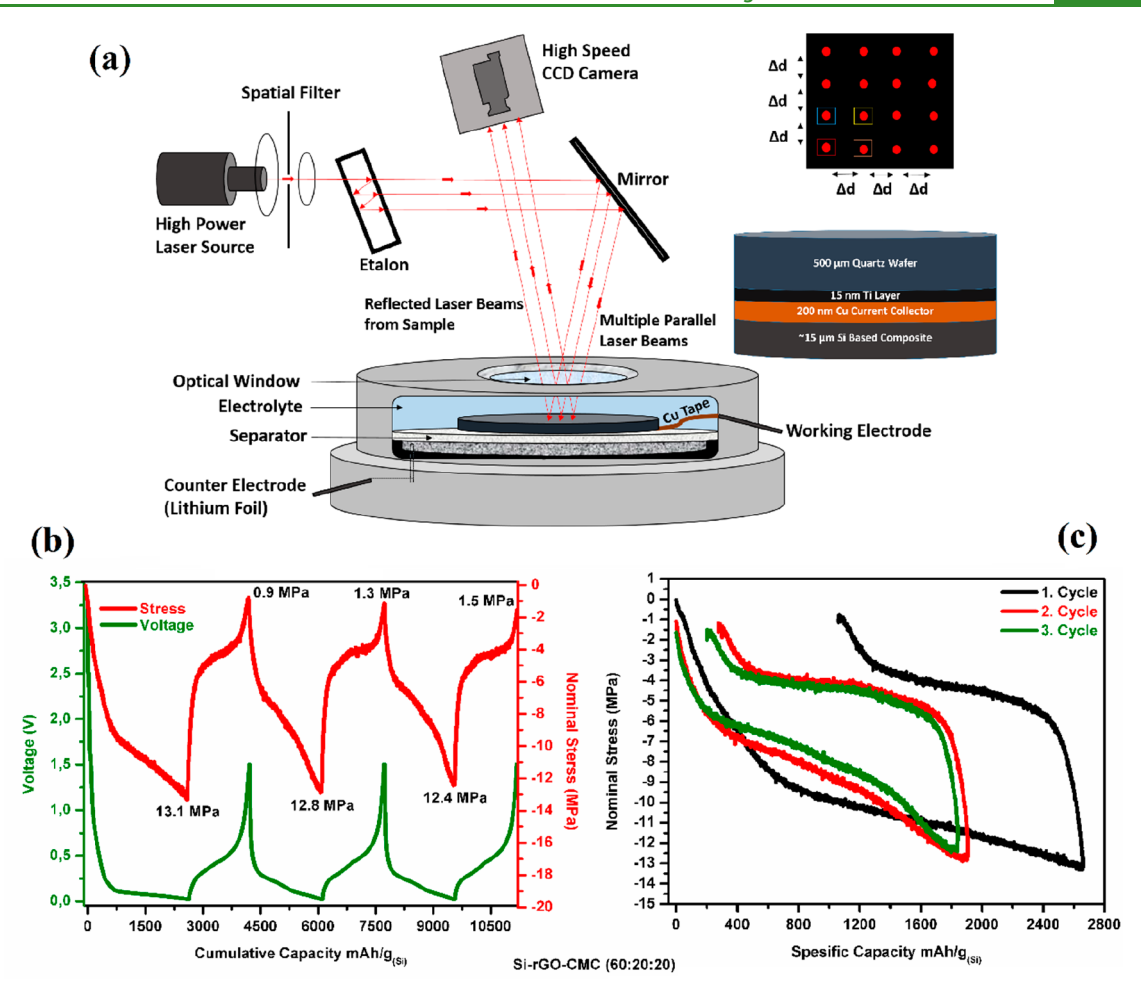


Figure 5. Schematic representation of MOSS system and custom-built electrochemical cell (a), real-time stress measurement of Si-rGO-CMC electrode during the initial three galvanostatic cycles (b), and hysteresis loop in the stress response (c).

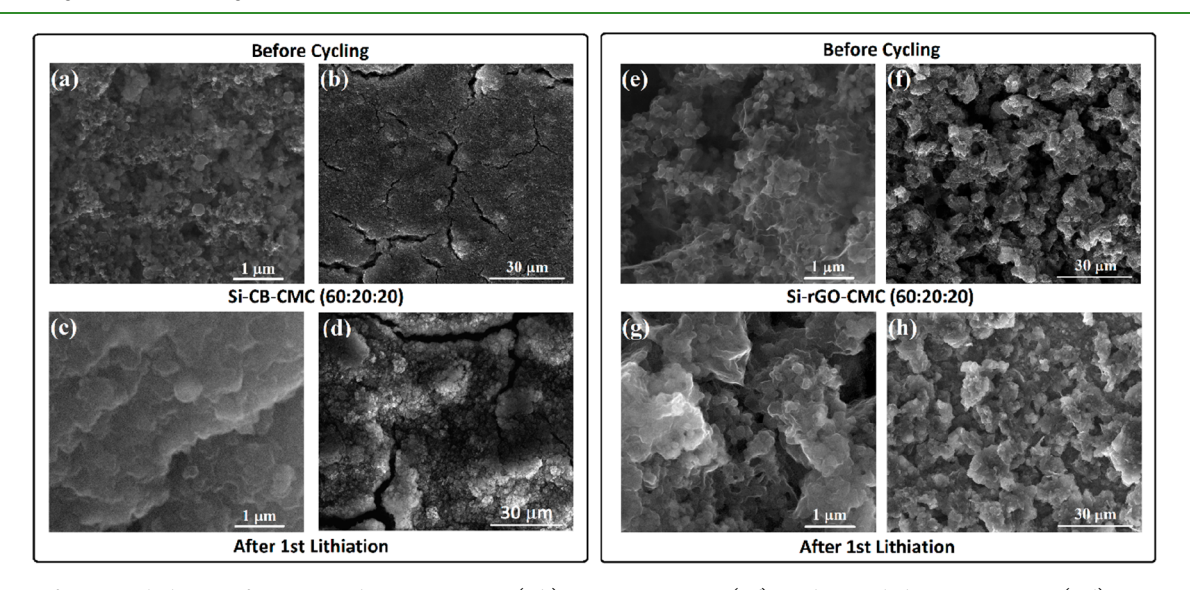


Figure 6. Surface morphologies of as-prepared Si–CB–CMC (a,b), Si–rGO–CMC (e,f), and as-cycled Si–CB–CMC (c,d), Si–rGO–CMC (g,h) composite electrodes.

was measured as 13.1 MPa, which was subsequently alleviated proportionally during delithiation. After the first full cycle, 0.9 MPa compressive stress remained in the electrode, depending on the high capacity of the first lithiation. The negligence of such a small irreversible stress is possible for Si-based

electrodes. It could be associated with the formation of SEI layer. Thus, dissipation of energy in the first cycle must be considered separately. The diffusion-induced stress evolution in the electrode was observed as stable during cycling without anomalous changes, which is consistent with an elastic

Table 2. Void Fraction (φ) Calculation of Si-CB-CMC and Si-rGO-CMC Electrodes

material properties	Si-CB-CMC (in Figure 2a)	Si-rGO-CMC (in Figure 2b)	Si-rGO-CMC (in Figure 2c)	Si-rGO-CMC (in Figure 2d)
total mass of electrode	1.3 mg	1.4 mg	1.4 mg	2.7 mg
fib thickness	$11~\mu\mathrm{m}$	8 μm	9 μm	$16~\mu\mathrm{m}$
area of electrode	1.26677 cm ²	1.26677 cm ²	1.26677 cm ²	1.26677 cm^2
$V_{ m Actual}$	$13.9345 \times 10^{-4} \text{ cm}^3$	$10.13416 \times 10^{-4} \text{ cm}^3$	$11.40093 \times 10^{-4} \text{ cm}^3$	$20.26832 \times 10^{-4} \text{ cm}^3$
density of Si	2.32 g/cm^3	2.32 g/cm^3	2.32 g/cm^3	2.32 g/cm^3
density of CMC	1.6 g/cm ³	1.6 g/cm ³	1.6 g/cm ³	1.6 g/cm^3
density of CB/rGO	1.7 g/cm ³	1.91 g/cm^3	1.91 g/cm^3	1.91 g/cm ³
mass of Si	$1.3 \times 0.6 = 0.78 \text{ mg}$	$1.4 \times 0.6 = 0.84 \text{ mg}$	$1.4 \times 0.6 = 0.84 \text{ mg}$	$2.7 \times 0.6 = 1.62 \text{ mg}$
mass of CMC	$1.3 \times 0.2 = 0.26 \text{ mg}$	$1.4 \times 0.2 = 0.28 \text{ mg}$	$1.4 \times 0.2 = 0.28 \text{ mg}$	$2.7 \times 0.6 = 0.54 \text{ mg}$
mass of CB/rGO	$1.3 \times 0.2 = 0.26 \text{ mg}$	$1.4 \times 0.2 = 0.28 \text{ mg}$	$1.4 \times 0.2 = 0.28 \text{ mg}$	$2.7 \times 0.6 = 0.54 \text{ mg}$
volume of Si	$3.362 \times 10^{-4} \text{ cm}^3$	$3.6207 \times 10^{-4} \text{ cm}^3$	$3.6207 \times 10^{-4} \text{ cm}^3$	$6.9828 \times 10^{-4} \text{ cm}^3$
volume of CMC	$1.625 \times 10^{-4} \text{ cm}^3$	$1.75 \times 10^{-4} \text{ cm}^3$	$1.75 \times 10^{-4} \text{ cm}^3$	$3.375 \times 10^{-4} \text{ cm}^3$
volume of CB/rGO	$1.529 \times 10^{-4} \text{ cm}^3$	$1.466 \times 10^{-4} \text{ cm}^3$	$1.466 \times 10^{-4} \text{ cm}^3$	$2.827 \times 10^{-4} \text{ cm}^3$
$V_{ m Theoretical}$	$6.516 \times 10^{-4} \text{ cm}^3$	$6.8367 \times 10^{-4} \text{ cm}^3$	$6.8367 \times 10^{-4} \text{ cm}^3$	$13.1848 \times 10^{-4} \text{ cm}^3$
$\emptyset_{ ext{Porosity}}$	0.5324	0.3254	0.4003	0.3495

response of Si-rGO composite. Reversible evolution of induced stress during cycling was also seen in hysteresis loops in Figure 5c. Steadiness of stress accumulation and release during successive delithiation and lithiation was ascribed with reversible structural changes (in elastic band) of the hybrid electrode since it is known the direct correlation between stress generation and structural change. To make an easy comparison, stress generation of Si-rGO composite was modeled with finite element modeler and solved with ANSYS STRUCTURAL in our previous study.⁴³ The aim was to calculate the effective stress that emerged between Si nanoparticles and rGO layers. In the case of 400% volume expansion of Si, the maximum equivalent stress was measured as 154.91 MPa on nanolayers. Here we monitored the realtime stress response of the whole electrode prepared with SirGO-CMC during lithium insertion and extraction processes. It is clearly seen that rGO layers can be capable to bear the mechanical stresses (from 154.91 to 13.1 MPa) transferred from Si nanoparticles. The volume expansion and stress results of Si-CB-CMC composite electrode with the same combination have already been reported by Kumar et al.³⁹ At the full lithiation stages, average in-plane stresses of this electrode range from ~100 to ~150 MPa which is almost 10 times higher than that of the Si-rGO-CMC electrode. This study proved that a successful wrapping of rGO on Si nanoparticles prominently contributes to the stress relaxation in the composite electrode.

Structural Changes. Surfaces morphologies of the distinct electrodes, examined by scanning electron microscopy before and after the first lithiation, are presented in Figure 6. Uniform and homogeneous close-packed surface morphology can be seen in the CB-containing electrode in Figure 6a,b. Nevertheless, the formation of large cracks on the whole electrode surface was observed before electrochemical cycling. These cracks are probably due to the high CMC binder content (20 wt %) and the fast-drying process. The crack spacings are much larger than the electrode thickness, and thus they do not substantially alter interpretation of the in situ stress measurements. Zhang et al. ⁵⁶ have shown that this type of cracking can be eliminated, but this type of process optimization study was not needed to achieve the primary goals of our current investigation.

The small active material particles (~100 nm) dispersed in the CB-CMC mixtures in the cycled electrodes were examined

at higher magnification. Figure 6c,d shows that these particles underwent huge volume expansion (~400%) with an average diameter of ~400 nm. Moreover, the cracks on the electrodes were also expanded after the cycling. Although, the surface cracking mostly encourages having an enlarged surface area which leads to facile Li+ transport, on the other hand SEI could be continuously formed on the newly exposed surface of the electrode, as a result of the cracking, which would negate the enhanced Li⁺ transport effect. SEM images of rGO-containing electrode with a rather uniform porous surface with no visible cracks are shown in Figure 6e,f. More porosity clearly can be observed when compared with the CB-containing electrode. Wrapping of all the active materials with rGO without any agglomeration was also imaged in higher magnification of the composite electrode. Interestingly, the persistence of the surface porosity, similar to a fresh electrode, is visible in the cycled electrode presented in Figure 6g,h. The volume expansion in particle size is about ~40% after the first lithiation which is 10 times greater than the CB-based electrode. Regarding a specific explanation when analyzing the electrode surfaces with low magnification, surface roughness of the rGO-containing electrode has shown to be much higher than that of the CB-containing electrode. However, a closer look at the electrodes has also detected that the rGOcontaining electrode has a smoother surface because of the presence of the rGO sheets that covered Si nanoparticles homogeneously.

The porosity of the composite electrodes plays an important role in the deformation that occurs during cycling. Void fractions of constituents were calculated by

$$\emptyset_{\text{Porosity}} = \frac{V_{\text{Actual}} - V_{\text{Theoretical}}}{V_{\text{Actual}}}$$
(3)

 $V_{\rm Actual}$ can be obtained from the electrode area and measured thickness with FIB. $V_{\rm Theoretical}$ must be calculated from the weights and the densities of components (Si, CB/rGO, and binder). All of the information about basic properties of materials were taken from the related literature for theoretical calculation and summarized in Table 2. On the basis of the equivalent three, void fractions of as-prepared composite electrodes were obtained at (Si–CB–CMC) 53.24% and (Si–rGO–CMC) 32.54%.

Interestingly, it was expected to find higher porosity for the rGO-containing electrode, because internal porosity can buffer

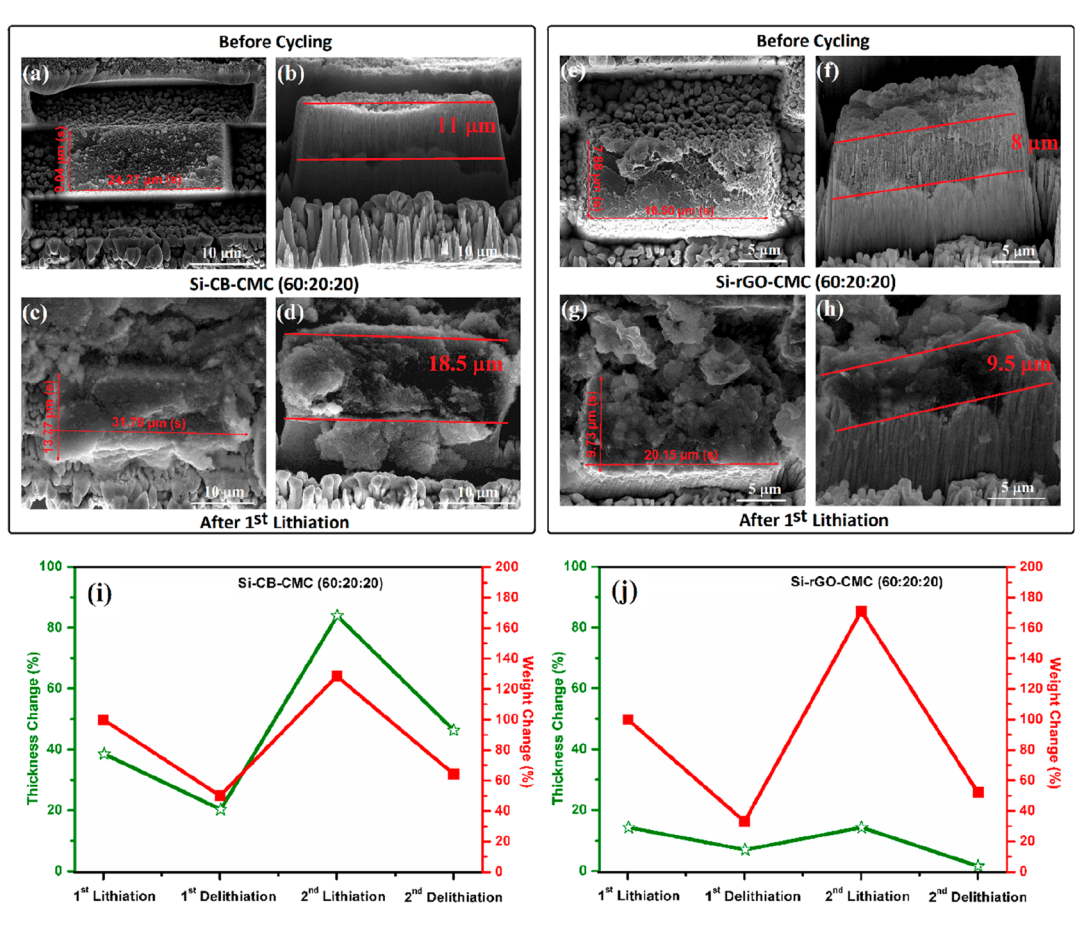


Figure 7. Island structures of composite electrodes fabricated with FIB. Surface and cross-sectional images of as-prepared Si–CB–CMC (a,b), as-cycled Si–CB–CMC (c,d), as-prepared Si–rGO–CMC (e,f), and as-cycled Si–rGO–CMC (g,h). Thickness (calculated with FIB) and weight changes (ex situ measurement) of Si–CB–CMC (i) and Si–rGO–CMC (j) composite electrodes during cycling. Electrodes were cycled with C/20.

the volume expansion of Si nanoparticles. However, the porosity of the Si-rGO-CMC electrode is almost 2 times lower than that of the Si-CB-CMC electrode. This unexpected result will be discussed further in the next sections.

To investigate the relationship between porosity level and electrochemical reversibility of the rGO containing electrodes, the same Si-rGO-CMC electrodes were prepared with different porosity and electrochemical charge-discharge tests were performed under the same conditions (C/20 current rate) given in Figure S6. The differences of capacities could be ascribed with the thickness of the electrodes. But the comparison is focused on the stability of the cells. Since it is really difficult to fully control the porosity of the electrodes during production, comparisons were made by measuring the porosities of the preprepared thickness-controlled electrodes (at least three tests for each electrode). The results show that lithiation capacities of all of the electrodes tend to increase in the initial cycles as expected from the rGO-based electrode presented in this study. However, the intensity and cycle number of the increment is varied depending on porosity levels. The capacities of the electrodes with the porosity of less than 30% are decreased after 15 cycles, which is similar to the CB-containing electrode presented in Figure 2a. One can assume that low porosity of the rGO networks may not accompany the volume expansion of Si for long cycles. On the other hand, the capacity decrease is not seen in the electrodes with 38% and 42% porosity levels for 50 cycles. Moreover,

capacity increase is continued slightly. Electrochemical stability of the cells containing the electrodes with a porosity of more than 60% is decreased dramatically after 30 cycles, which is most likely due to an increase of the charge transfer resistance between conductive materials and active materials. On the basis of these results, since the quantitative value is hard to determine the optimum porosity level of the Si-rGO-CMC (60:20:20) based electrode can be suggested as being between 35% and 45%.

In order to see the strain in the lithium ion cell, ex situ analysis of composite electrodes was carried out after the first full lithiation (cycled with C/20). Island structures were fabricated with focused ion beam (FIB) to determine the film thicknesses and volume changes. It was aimed create some spaces to lead free expansion via the Ga-ion milling. As displayed in Figure 7a-h, the thicknesses of composite films were highlighted with red arrows. Because of the rough surface of copper foil, the average thicknesses were given on the islands. To better understand the elemental composition and the distribution of the composite film, MAP and line analysis of the Si-rGO-CMC island were examined in Figure S7. The thickness of the composite film $(7-8 \mu m)$ was presented with line analysis. The green region demonstrates the existence of Si nanoparticles in coated composite film while the blue area represents the presence of Cu foil in the MAP image. Vertical and horizontal expansion of islands as well as the total volume change of the electrodes were calculated before cycling and

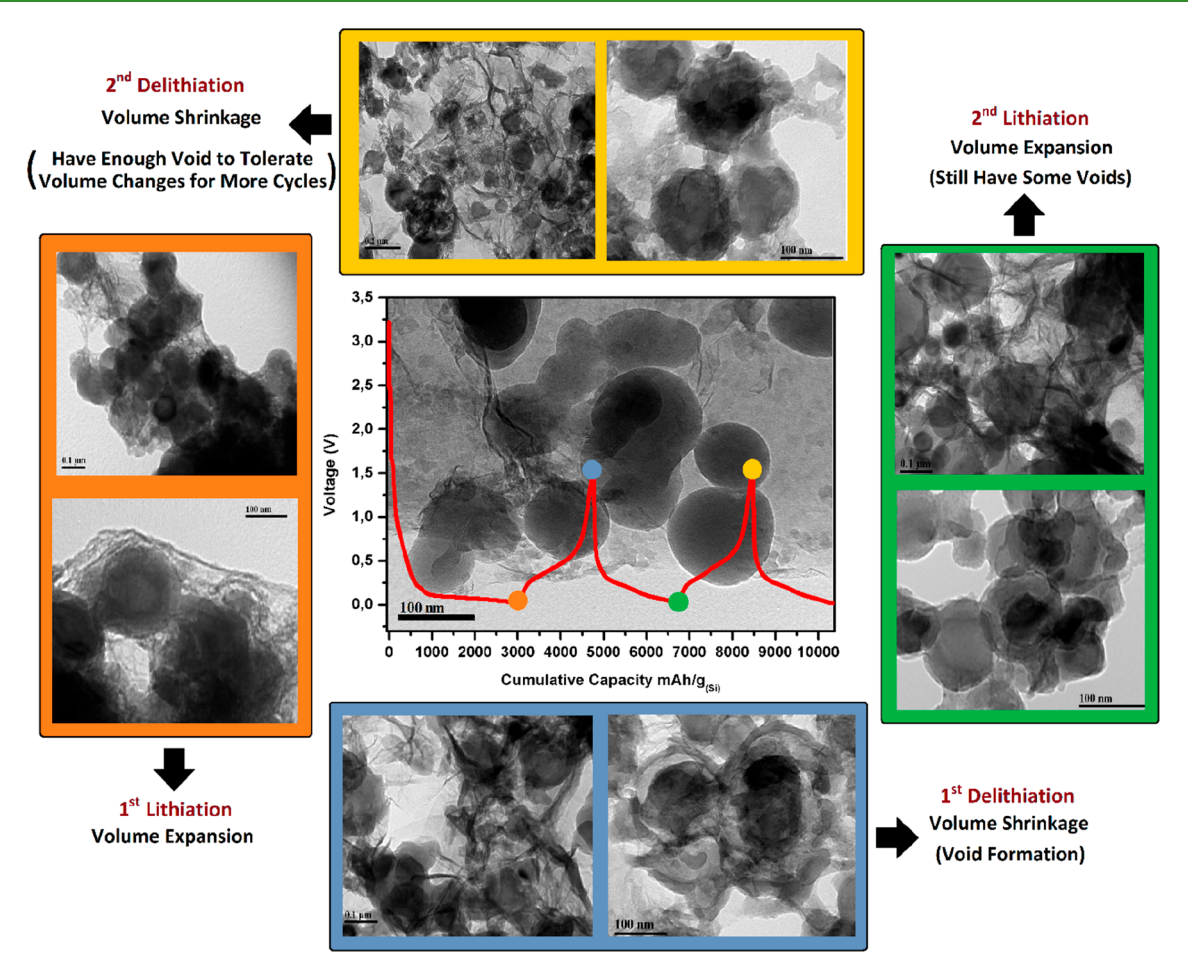
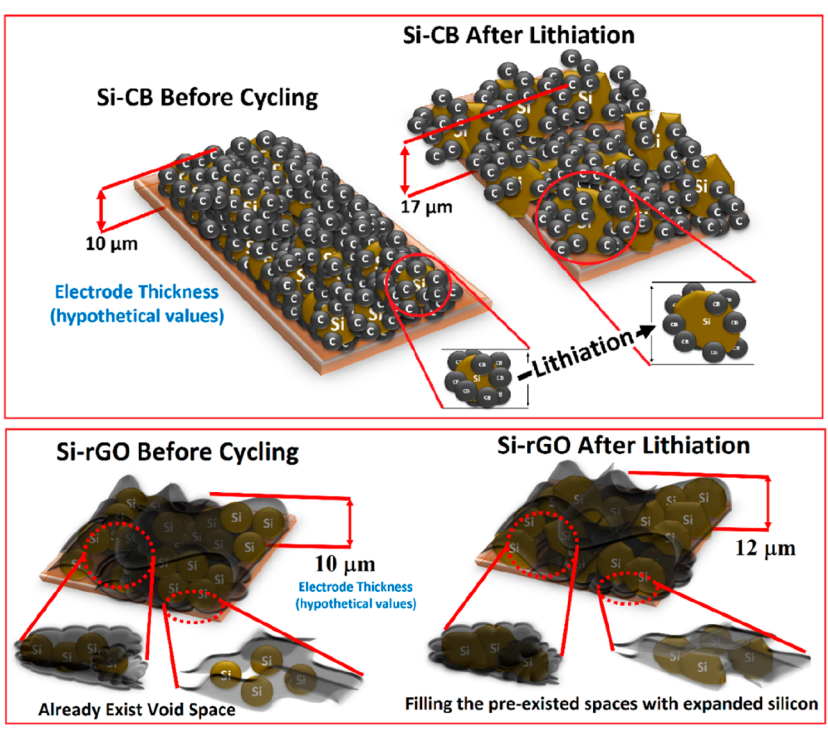


Figure 8. TEM images of as-prepared and as-cycled Si-rGO-CMC electrodes.

after the first lithiation. As can be seen in Figure 7a-d, island thickness of Si-CB-CMC was changed from 11 to 18.5 μ m; that means an ~68% thickness change occurred after the first full lithiation. When combining the thickness with lateral expansion of the island, the volumetric change was calculated as ~235.45%. Figure 7e-h shows the island structures of SirGO-CMC electrode before and after lithiation. Similarly, during lithiation vertical and horizontal expansion of the island is evident. However, the thickness change of the Si-rGO-CMC island was observed at ~18.75%. In addition, the total volume change of this island was found at ~59.7%. The aforementioned results indicated that strain relaxation was improved almost 4 times by using rGO in the Si-based composite electrode. It is important to note that both composite films appeared well adhered to the Cu foil current collector before cycling. However, peeling of the Si-CB-CMC composite film was detected after lithiation (in Figure 7d) due to a huge volume change and large stress evolution of the electrode. A closer presentation of this situation is also given in Figure S4. This problem could result in contact loss between current collector and active material for long cycles. Structural and electrochemical analysis of the MOSS electrode (discussed in Figure 5) before cycling and after the fourth lithiation is also given in Figure S8. XRD and FIB results are similar to the conventional method displayed in this study. The lithiation products of Li₂CO₃, Li₂₁Si₈, Li₁₂Si₇ and LiF, are detected in XRD after the fourth lithiation. The peaks representing crystalline Si are still observed but rather weak. The electrode thickness determined by FIB, which was 12 μ m

before cycling, is observed to be 14 μ m after the fourth lithiation. So, the total change in thickness was calculated to be about 17% which is a very promising result for the further electrochemical reaction and structural stability in LIB.

The performance of LIBs is strongly affected by the large volume change of the electrodes. There are many challenges related to the expansion and contraction of silicon particles during cycling, such as the formation of uncontrolled SEI. increased internal resistance, and stress generation. All of these can result in capacity loss in lithium ion cells. Information about overall volume changes was investigated by measuring the thickness change of composite electrodes before cycling and after first lithiation, first delithiation, second lithiation, and second delithiation. These comparisons carried out on the electrodes are shown in Figure 7i,j. Electrode cutting was performed with FIB before electrochemical cycling and measured the film thickness from cross-sectional view characterized by SEM. Calculations were carried out at the same regions to see the real change after some lithiation and delithiation. Different electrodes (but the same combination, thickness, and weights) were prepared for each analysis and cycled under the same conditions. It is shown that the thickness change of the CB-containing electrode is ~40% before the first lithiation and decreased to ~20% after the first delithiation. That means $\sim 20\%$ thickness change remained in the electrode shown in Figure 7i. Irreversible changes cause the internal stress and increase the resistance of the electrode. Thickness change difference is observed between the two electrodes. A change of ~14% was evidenced for the rGO-



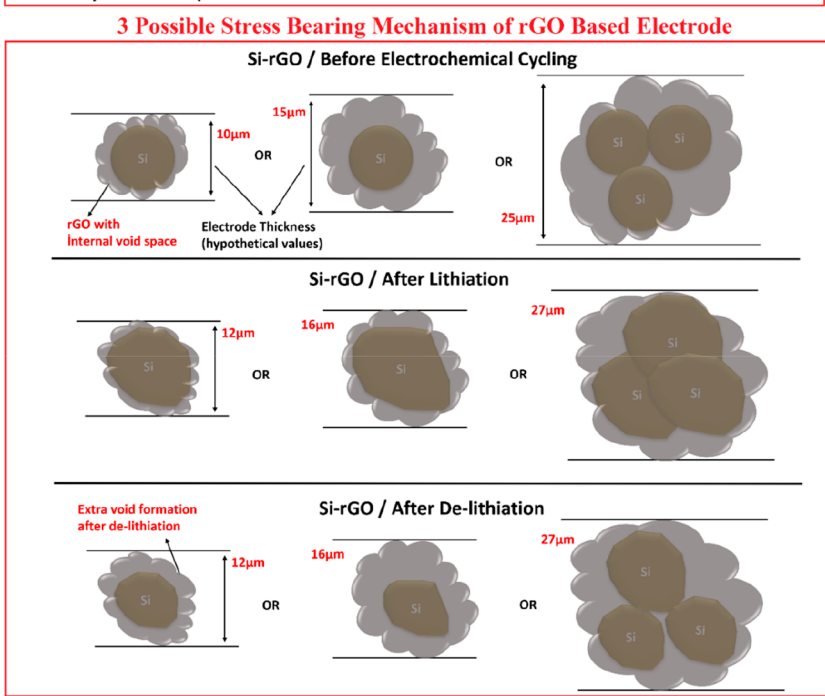


Figure 9. Stress mechanism of silicon-based composite electrodes and stress-bearing mechanism of rGO-based electrodes.

containing electrode in Figure 7j, and it decreased to \sim 7% after the first delithiation. The reason for this difference between the two electrodes can be ascribed to SEI formation on the surface of the Si nanoparticles. Because of the wrapping effect in the Si–rGO–CMC electrodes, the Si nanoparticles were not directly exposed to the electrolyte. The impact on limiting SEI formation depends on the rGO layer thickness. After two cycles, \sim 46% thickness change for the CB-containing electrode (which is an extra \sim 26% thickness change after the first cycle) and \sim 1.6% thickness change for the rGO-containing-electrode were detected. After the results of the ex situ thickness analysis, the rGO provides a buffer layer to compensate the volume

expansion and to enhance the structural stability of electrodes. The results related to the thickness change in the rGO-based electrodes were confirmed with TEM analysis and discussed using a model of the structural changes that is described further below.

The weight fraction of the electrodes was measured to provide information about the lithium ion diffusion during cycling. The mass loading of the as-prepared electrodes was almost similar. Lithium ion diffusion into the working electrode (i.e., alloying with Si) increases the electrode weight, which subsequently decreases proportionally during the delithiation process. Thus, investigating the weight fraction

of the electrode confirms that the rGO-containing electrodes were successfully lithiated and delithiated with high capacity (2738 mAhg⁻¹ after 30 cycles at C/20 rate), but without huge stress generated in the electrode. Briefly, the weight of both prepared electrodes increased and decreased regularly during lithiation and delithiation processes. Interestingly, although the thickness change and stress formation of the electrode containing the rGO are lower, the weight change of this electrode is observed on a larger scale during the electrochemical cycles. This not only demonstrates the electrochemical performance of the electrode containing the rGO but it also explains the difference in capacity in the charge—discharge tests.

The reversible volume change of Si in the Si-rGO-CMC electrode was further confirmed with TEM images, as shown in Figure 8. Cumulative capacity versus voltage plots along with the TEM image of the as-prepared electrode are shown in the middle of the figure. The solid circles in the graph identify different steps in the cycling process. Ex situ TEM images of cycled electrodes indicate that the volume change in the rGOcontaining electrodes is regular and reversible during cycling. Voids in the as-prepared electrode facilitate electrolyte penetration and ion diffusion. After lithiation, Si nanoparticles were expanded and connected strongly with rGO layers. The better connection of these particles improves electron conductivity, contributes to fast charge transfer, and enhances lithium incorporation. During delithiation, the Si nanoparticles contracted and created voids between particles and layers. This fascinating result provides insight into how free space is created for subsequent Si swelling, while protecting the overall structural stability of the electrode against large volume variations. This is consistent with the lower internal resistance observed in the rGO-based electrodes and with the 3D wrapping of the rGO layers that is retained in the electrode.

Stress Mechanism. Lithiation-induced stress evolutions in the different electrodes are depicted in Figure 9. Three possible stress-bearing mechanisms of the Si-rGO composite are also proposed here. In the case of Si-CB, the thickness of the electrode strongly depends on the Si nanoparticles. After lithiation, all of the Si nanoparticles expand together, and this results in a large increase in the electrode thickness (shown in the schematic). Because of the deeply heterogeneous volume changes, Li⁺ ion diffusion inside the electrode is hindered and there is a significant increase in impedance, which is consistent with Figure 3a.

The overall thickness of the Si-rGO electrodes are also directly related to the architectures that were produced in this work. There are three important components in these Si-rGO materials: Si@void@rGO layers. The void mechanism here can be used to form variable electrode microstructures. Models for three different situations commonly seen in the Si-rGO systems are presented in Figure 9 to better understand the stress-bearing mechanism of the rGO network. In the first situation, limited void space can be seen around the Si particle. During lithiation, the expansion of the Si particle increases the contact pressure between Si and rGO, which leads to expansion of the flexible rGO layers, depending on the degree of lithiation. After delithiation, the alloyed particles shrink between the layers. This cycle process creates more void around the Si. These rGO layers are highly flexible, and thus we believe that the electrode stability during cycling is due to the conformational transformation of the wavy surfaces during Si alloying. This is consistent with the TEM images in Figure 8.

Volume changes occur in this void in the next cycles without leading to larger deformation and mechanical degradation of the electrode. As also stated in Figure 3b, the electrochemical results concerning the impedance measurements are rather stable during the first 50 cycles. In situ stress measurements and ex situ microstructural evolution analyses are consistent with this. In the second situation, there is already enough space to accommodate the volume change in the rGO bubble. Because of this, volume expansion of Si does not significantly increase the electrode thickness. The pre-existing porous structure between Si and rGO preserves the structural integrity of electrode materials and prevents capacity fade. In the third situation, it is also possible to observe the wrapping of more than one Si particle between the layers. These particles can expand or shrink together in the bubble. These contacting Si particles can also agglomerate between the rGO layers, but this was minimized by the Si surface modification with APTES. In all of the situations depicted here, the thickness change of the electrode is relatively small, especially during cycles after the first lithiation. As a result, the advantages of all of these features in the lithium ion cell provide (i) good structural stability, (ii) improved mechanical integrity, and (iii) better electrochemical stability.

CONCLUSIONS

This study provides the first real-time stress measurements of Si-rGO-based composite electrodes during electrochemical cycling using a multibeam optical stress sensor. In order to better understand the improved electrochemical and mechanical behavior with these materials, the CB-containing composite electrodes were compared with analogous rGOcontaining composite electrodes. The measured stresses were correlated with electrochemical, structural, and phase evolution via combined SEM, TEM, FIB, and XRD. Internal resistances, electrochemical cycling results, and structural changes in the electrodes were all substantially improved in the Si-rGO-based composite electrode, demonstrating that these materials can deliver large capacity with good cycling stability. The average discharge capacity of the rGO-based electrode was double that of the CB-based electrode with average thickness changes that were a factor of 2 smaller. Moreover, reversible stress change was achieved with the Si-rGO composites, which can be attributed to the wrapping of the Si particles by the rGO nanolayers. Even though the porosity of the Si-CB-based electrode was higher than that of the Si-rGO-based electrode, the stresses in the Si-rGO-based electrode were much higher than those in the Si-CB based electrodes. To investigate the electrochemical impact of porosity in the rGO-based electrode, charge-discharge tests were also performed on electrodes with different porosity levels. The impact of porosity in the rGOcontaining electrodes was also assessed with basic models of deformation processes and stress-bearing mechanisms. These are aligned with the in situ and ex situ measurements, which indicate that the LIB performance was greatly improved by using rGO in Si-based electrodes. We believe this study may open new and effective routes for understanding and controlling stress-generating mechanisms of rGO-based composite electrodes in LIBs.

ASSOCIATED CONTENT

Supporting Information

The Supporting Information is available free of charge at https://pubs.acs.org/doi/10.1021/acsami.0c10064.

Figures S1 to S9 (PDF)

Stress distribution in rGO while 300% expansion of Si in case of \sim 40% porosity (MP4)

Bending structure and total deformation of single rGO layer; note: rGO sheets were modeled with beam analogy as one layer via finite elements method (MP4)

AUTHOR INFORMATION

Corresponding Author

Mahmud Tokur — Engineering Faculty, Department of Metallurgical and Materials Engineering, Research, Development and Application Center, and NESSTEC Energy and Surface Technologies A.S., Technology Development Zones, Sakarya University, 54050 Sakarya, Turkey; School of Engineering, Brown University, Providence, Rhode Island 02912, United States; orcid.org/0000-0003-3612-5350; Email: mtokur@sakarya.edu.tr

Authors

Mok Yun Jin — School of Engineering, Brown University, Providence, Rhode Island 02912, United States

Brian W. Sheldon – School of Engineering, Brown University, Providence, Rhode Island 02912, United States; occid.org/0000-0002-9593-891X

Hatem Akbulut — Engineering Faculty, Department of Metallurgical and Materials Engineering, Research, Development and Application Center, and NESSTEC Energy and Surface Technologies A.S., Technology Development Zones, Sakarya University, 54050 Sakarya, Turkey

Complete contact information is available at: https://pubs.acs.org/10.1021/acsami.0c10064

Notes

The authors declare no competing financial interest.

ACKNOWLEDGMENTS

This work is supported by the Scientific and Technological Research Council of Turkey (TUBITAK) for distinguished young scholars under the contract number 1059B141601245. The authors thank the TUBITAK BIDEB workers for their financial support. The authors also thank to TUBITAK TEYDEB-BIGG-1512 program for their financial support under the contract number 2190317. We also acknowledge support from the National Science Foundation, Ceramics Program (DMR-1832829)

■ REFERENCES

- (1) Zubi, G.; Dufo-López, R.; Carvalho, M.; Pasaoglu, G. The Lithium-Ion Battery: State of the Art and Future Perspectives. Renewable Sustainable Energy Rev. 2018, 89, 292–308.
- (2) Zhu, B.; Liu, G.; Lv, G.; Mu, Y.; Zhao, Y.; Wang, Y.; Li, X.; Yao, P.; Deng, Y.; Cui, Y.; Zhu, J. Minimized Lithium Trapping by Isovalent Isomorphism for High Initial Coulombic Efficiency of Silicon Anodes. *Sci. Adv.* **2019**, *5* (11), eaax0651.
- (3) Zheng, T.; Zhang, T.; de la Fuente, M. S.; Liu, G. Aqueous Emulsion of Conductive Polymer Binders for Si Anode Materials in Lithium Ion Batteries. *Eur. Polym. J.* **2019**, *114*, 265–270.
- (4) Jin, Y.; Liu, K.; Lang, J.; Jiang, X.; Zheng, Z.; Su, Q.; Huang, Z.; Long, Y.; Wang, C. an; Wu, H.; Cui, Y. High-Energy-Density Solid-Electrolyte-Based Liquid Li-S and Li-Se Batteries. *Joule* **2020**, *4* (1), 262–274.
- (5) Wang, H.; Fu, J.; Wang, C.; Wang, J.; Yang, A.; Li, C.; Sun, Q.; Cui, Y.; Li, H. A Binder-Free High Silicon Content Flexible Anode for Li-Ion Batteries. *Energy Environ. Sci.* **2020**, *13*, 848–858.

- (6) Ko, M.; Chae, S.; Ma, J.; Kim, N.; Lee, H. W.; Cui, Y.; Cho, J. Scalable Synthesis of Silicon-Nanolayer-Embedded Graphite for High-Energy Lithium-Ion Batteries. *Nat. Energy* **2016**, *1* (9), 1–8.
- (7) Ababtain, K.; Babu, G.; Susarla, S.; Gullapalli, H.; Masurkar, N.; Ajayan, P. M.; Arava, L. M. R. Porous Graphene Current Collectors Filled with Silicon as High-Performance Lithium Battery Anode. *Mater. Res. Express* **2018**, *5* (1), 014004–014011.
- (8) Ren, W. F.; Li, J. T.; Zhang, S. J.; Lin, A. L.; Chen, Y. H.; Gao, Z. G.; Zhou, Y.; Deng, L.; Huang, L.; Sun, S. G. Fabrication of Multi-Shell Coated Silicon Nanoparticles via in-Situ Electroless Deposition as High Performance Anodes for Lithium Ion Batteries. *J. Energy Chem.* **2020**, *48*, 160–168.
- (9) Baasner, A.; Reuter, F.; Seidel, M.; Krause, A.; Pflug, E.; Härtel, P.; Dörfler, S.; Abendroth, T.; Althues, H.; Kaskel, S. The Role of Balancing Nanostructured Silicon Anodes and NMC Cathodes in Lithium-Ion Full-Cells with High Volumetric Energy Density. *J. Electrochem. Soc.* **2020**, *167* (2), 020516–020527.
- (10) Jiao, M.-l.; Qi, J.; Shi, Z.-q.; Wang, C.-y. Three-Dimensional Si/Hard-Carbon/Graphene Network as High-Performance Anode Material for Lithium Ion Batteries. *J. Mater. Sci.* **2018**, 53 (3), 2149–2160
- (11) Li, R.; Li, J.; Qi, K.; Ge, X.; Zhang, Q.; Zhang, B. One-Step Synthesis of 3D Sulfur/Nitrogen Dual-Doped Graphene Supported Nano Silicon as Anode for Li-Ion Batteries. *Appl. Surf. Sci.* **2018**, 433, 367–373.
- (12) Zhang, W.; Cai, T. H.; Sheldon, B. W. The Impact of Initial SEI Formation Conditions on Strain-Induced Capacity Losses in Silicon Electrodes. *Adv. Energy Mater.* **2018**, *9* (5), 1803066.
- (13) Wang, G.; Xu, B.; Shi, J.; Lei, X.; Ouyang, C. Confined Li Ion Migration in the Silicon-Graphene Complex System: An Ab Initio Investigation. *Appl. Surf. Sci.* **2018**, *436* (2010), 505–510.
- (14) Liu, Y.; Wan, H.; Liu, S.; Zheng, S.; Dou, A.; Su, M. Facile Preparation of SGC Composite as Anode for Lithium-Ion Batteries. *Ionics* **2018**, 24 (9), 2575–2581.
- (15) Haregewoin, A. M.; Terborg, L.; Zhang, L.; Jurng, S.; Lucht, B. L.; Guo, J.; Ross, P. N.; Kostecki, R. The Electrochemical Behavior of Poly 1-Pyrenemethyl Methacrylate Binder and Its Effect on the Interfacial Chemistry of a Silicon Electrode. *J. Power Sources* **2018**, 376, 152–160.
- (16) Wang, M. S.; Wang, Z. Q.; Jia, R.; Yang, Y.; Zhu, F. Y.; Yang, Z. L.; Huang, Y.; Li, X.; Xu, W. Facile Electrostatic Self-Assembly of Silicon/Reduced Graphene Oxide Porous Composite by Silica Assist as High Performance Anode for Li-Ion Battery. *Appl. Surf. Sci.* **2018**, 456, 379—389.
- (17) Yang, D.; Shi, J.; Shi, J.; Yang, H. Simple Synthesis of Si/Sn@C-G Anodes with Enhanced Electrochemical Properties for Li-Ion Batteries. *Electrochim. Acta* **2018**, 259, 1081–1088.
- (18) Bae, J.; Kim, D. S.; Yoo, H.; Park, E.; Lim, Y. G.; Park, M. S.; Kim, Y. J.; Kim, H. High-Performance Si/SiOx Nanosphere Anode Material by Multipurpose Interfacial Engineering with Black TiO2-X. ACS Appl. Mater. Interfaces 2016, 8 (7), 4541–4547.
- (19) Wu, C.; Lin, J.; Chu, R.; Zheng, J.; Chen, Y.; Zhang, J.; Guo, H. Reduced Graphene Oxide as a Dual-Functional Enhancer Wrapped over Silicon/Porous Carbon Nanofibers for High-Performance Lithium-Ion Battery Anodes. J. Mater. Sci. 2017, 52 (13), 7984—7996.
- (20) Huang, Y.; Yang, H.; Xiong, T.; Adekoya, D.; Qiu, W.; Wang, Z.; Zhang, S.; Balogun, M.-S. Adsorption energy engineering of nickel oxide hybrid nanosheets for high areal capacity flexible lithium-ion batteries. *Energy Storage Mater.* **2020**, *25*, 41–51.
- (21) Bogart, T. D.; Oka, D.; Lu, X.; Gu, M.; Wang, C.; Korgel, B. A. Lithium Ion Battery Peformance of Silicon Nanowires with Carbon Skin. *ACS Nano* **2014**, *8* (1), 915–922.
- (22) Kim, B.; Ahn, J.; Oh, Y.; Tan, J.; Lee, D.; Lee, J. K.; Moon, J. Highly Porous Carbon-Coated Silicon Nanoparticles with Canyon-like Surfaces as a High-Performance Anode Material for Li-Ion Batteries. *J. Mater. Chem. A* **2018**, *6* (7), 3028–3037.
- (23) Liu, Z.; Guan, D.; Yu, Q.; Xu, L.; Zhuang, Z.; Zhu, T.; Zhao, D.; Zhou, L.; Mai, L. Monodisperse and Homogeneous SiOx/C Microspheres: A Promising High-Capacity and Durable Anode

- Material for Lithium-Ion Batteries. *Energy Storage Mater.* **2018**, *13*, 112–118.
- (24) Chakrapani, V.; Rusli, F.; Filler, M. A.; Kohl, P. A. Silicon Nanowire Anode: Improved Battery Life with Capacity-Limited Cycling. *J. Power Sources* **2012**, 205, 433–438.
- (25) Gohier, A.; Laïk, B.; Kim, K. H.; Maurice, J. L.; Pereira-Ramos, J. P.; Cojocaru, C. S.; Van, P. T. High-Rate Capability Silicon Decorated Vertically Aligned Carbon Nanotubes for Li-Ion Batteries. *Adv. Mater.* **2012**, *24* (19), 2592–2597.
- (26) Li, Z. F.; Zhang, H.; Liu, Q.; Liu, Y.; Stanciu, L.; Xie, J. Novel Pyrolyzed Polyaniline-Grafted Silicon Nanoparticles Encapsulated in Graphene Sheets as Li-Ion Battery Anodes. ACS Appl. Mater. Interfaces 2014, 6 (8), 5996–6002.
- (27) Wu, P.; Wang, H.; Tang, Y.; Zhou, Y.; Lu, T. Three-Dimensional Interconnected Network of Graphene-Wrapped Porous Silicon Spheres: In Situ Magnesiothermic-Reduction Synthesis and Enhanced Lithium-Storage Capabilities. ACS Appl. Mater. Interfaces 2014, 6 (5), 3546–3552.
- (28) Tokur, M.; Algul, H.; Ozcan, S.; Cetinkaya, T.; Uysal, M.; Akbulut, H. Closing to Scaling-Up High Reversible Si/RGO Nanocomposite Anodes for Lithium Ion Batteries. *Electrochim. Acta* **2016**, 216, 312–319.
- (29) Xu, Q.; Sun, J. K.; Li, J. Y.; Yin, Y. X.; Guo, Y. G. Scalable Synthesis of Spherical Si/C Granules with 3D Conducting Networks as Ultrahigh Loading Anodes in Lithium-Ion Batteries. *Energy Storage Mater.* **2018**, *12*, 54–60.
- (30) Kim, S. K.; Chang, H.; Kim, C. M.; Yoo, H.; Kim, H.; Jang, H. D. Fabrication of Ternary Silicon-Carbon Nanotubes-Graphene Composites by Co-Assembly in Evaporating Droplets for Enhanced Electrochemical Energy Storage. *J. Alloys Compd.* **2018**, *751*, 43–48.
- (31) Chiu, K. F.; Lai, P. Recycled Crystalline Micro-Sized Silicon Particles Modified by Pyrolytic Coatings Using Poly(Ether Ether Ketone) Precursor for Stable Lithium Ion Battery Anodes. *Mater. Sci. Eng., B* **2018**, 228, 52–59.
- (32) Kim, H.-s.; Kim, J.; Lee, J. G.; Ryu, J. H.; Kim, J.; Oh, S. M.; Yoon, S. Novel Silicon—Tungsten Oxide—Carbon Composite as Advanced Negative Electrode for Lithium-Ion Batteries. *Solid State Ionics* **2018**, *314*, 41–45.
- (33) Tao, H.; Xiong, L.; Zhu, S.; Zhang, L.; Yang, X. Porous Si/C/Reduced Graphene Oxide Microspheres by Spray Drying as Anode for Li-Ion Batteries. *J. Electroanal. Chem.* **2017**, *797*, 16–22.
- (34) Zhang, C.; Kang, T. H.; Yu, J. S. Three-Dimensional Spongy Nanographene-Functionalized Silicon Anodes for Lithium Ion Batteries with Superior Cycling Stability. *Nano Res.* **2018**, *11* (1), 233–245
- (35) Xie, H.; Kang, Y.; Song, H.; Zhang, Q. Real-Time Measurements and Experimental Analysis of Material Softening and Total Stresses of Si-Composite Electrode. *J. Power Sources* **2019**, 424, 100–107.
- (36) Zhou, Y.; Yang, Y.; Hou, G.; Yi, D.; Zhou, B.; Chen, S.; Lam, T. D.; Yuan, F.; Golberg, D.; Wang, X. Stress-Relieving Defects Enable Ultra-Stable Silicon Anode for Li-Ion Storage. *Nano Energy* **2020**, *70*, 104568–104579.
- (37) Cao, L.; Yang, H.; Fan, F. Stress Generation during Anisotropic Lithiation in Silicon Nanopillar Electrodes: A Reactive Force Field Study. *Phys. Lett. A* **2019**, 383 (33), 125955–125960.
- (38) Deluca, C. M.; Maute, K.; Dunn, M. L. Effects of Electrode Particle Morphology on Stress Generation in Silicon during Lithium Insertion. *J. Power Sources* **2011**, *196* (22), 9672–9681.
- (39) Kumar, R.; Woo, J. H.; Xiao, X.; Sheldon, B. W. Internal Microstructural Changes and Stress Evolution in Silicon Nanoparticle Based Composite Electrodes. *J. Electrochem. Soc.* **2017**, *164* (14), A3750–A3765.
- (40) Jangid, M. K.; Mukhopadhyay, A. Real-Time Monitoring of Stress Development during Electrochemical Cycling of Electrode Materials for Li-Ion Batteries: Overview and Perspectives. *J. Mater. Chem. A* **2019**, 7 (41), 23679–23726.
- (41) Meng, T.; Li, B.; Wang, Q.; Hao, J.; Huang, B.; Gu, F. L.; Xu, H.; Liu, P.; Tong, Y. Large-Scale Electric-Field Confined Silicon with

- Optimized Charge-Transfer Kinetics and Structural Stability for High-Rate Lithium-Ion Batteries. ACS Nano 2020, 14, 7066.
- (42) Özcan, Ş.; Cetinkaya, T.; Tokur, M.; Algül, H.; Guler, M. O.; Akbulut, H. Synthesis of Flexible Pure Graphene Papers and Utilization as Free Standing Cathodes for Lithium-Air Batteries. *Int. J. Hydrogen Energy* **2016**, *41* (23), 9796–9802.
- (43) Tokur, M.; Aydin, A.; Cetinkaya, T.; Akbulut, H. Shoring up the Lithium Ion Batteries with Multi-Component Silicon Yolk-Shell Anodes for Grid-Scale Storage Systems: Experimental and Computational Mechanical Studies. *J. Electrochem. Soc.* 2017, 164 (9), A2238–A2250
- (44) Stankovich, S.; Dmitriy, A. D.; Richard, D. P.; Kevin, A. K.; Alfred, K.; Yuanyuan, J.; Yue, W.; SonBinh, T. N.; Rodney, S. R. Synthesis of graphene-based nanosheets via chemical reduction of exfoliated graphite oxide. *Carbon* **2007**, *45* (7), 1558–1565.
- (45) Pei, S.; Zhao, J.; Du, J.; Ren, W.; Cheng, H. M. Direct Reduction of Graphene Oxide Films into Highly Conductive and Flexible Graphene Films by Hydrohalic Acids. *Carbon* **2010**, 48 (15), 4466–4474.
- (46) Soni, S. K.; Sheldon, B. W.; Xiao, X.; Verbrugge, M. W.; Dongjoon, A.; Huajian, G.; et al. Stress mitigation during the lithiation of patterned amorphous Si islands. *J. Electrochem. Soc.* **2011**, *159* (1), A38–A43.
- (47) Mukhopadhyay, A.; Tokranov, A.; Xiao, X.; Sheldon, B. W. Stress Development Due to Surface Processes in Graphite Electrodes for Li-Ion Batteries: A First Report. *Electrochim. Acta* **2012**, *66*, 28–37.
- (48) Chabot, V.; Feng, K.; Park, H. W.; Hassan, F. M.; Elsayed, A. R.; Yu, A.; Xiao, X.; Chen, Z. Graphene Wrapped Silicon Nanocomposites for Enhanced Electrochemical Performance in Lithium Ion Batteries. *Electrochim. Acta* **2014**, *130*, 127–134.
- (49) Ko, M.; Chae, S.; Jeong, S.; Oh, P.; Cho, J. Elastic a -Silicon Nanoparticle Backboned Graphene Hybrid as a Self-Compacting Anode for High-Rate Lithium Ion Batteries. *ACS Nano* **2014**, *8* (8), 8591–8599.
- (50) Liu, N.; Lu, Z.; Zhao, J.; Mcdowell, M. T.; Lee, H. W.; Zhao, W.; Cui, Y. A Pomegranate-Inspired Nanoscale Design for Large-Volume-Change Lithium Battery Anodes. *Nat. Nanotechnol.* **2014**, 9 (3), 187–192.
- (51) Danet, J.; Brousse, T.; Rasim, K.; Guyomard, D.; Moreau, P. Valence Electron Energy-Loss Spectroscopy of Silicon Negative Electrodes for Lithium Batteries. *Phys. Chem. Chem. Phys.* **2010**, *12* (1), 220–226.
- (52) Zhao, J.; Liao, L.; Shi, F.; Lei, T.; Chen, G.; Pei, A.; Sun, J.; Yan, K.; Zhou, G.; Xie, J.; Liu, C.; Li, Y.; Liang, Z.; Bao, Z.; Cui, Y. Surface Fluorination of Reactive Battery Anode Materials for Enhanced Stability. *J. Am. Chem. Soc.* **2017**, *139* (33), 11550–11558.
- (53) Wang, Y.; Dahn, J. Phase Changes in Electrochemically Lithiated Silicon at Elevated Temperature. *J. Electrochem. Soc.* **2006**, 153 (12), A2314–A2318.
- (54) Whiteley, J. M.; Kim, J. W.; Piper, D. M.; Lee, S.-H. High-Capacity and Highly Reversible Silicon-Tin Hybrid Anode for Solid-State Lithium-Ion Batteries. *J. Electrochem. Soc.* **2016**, *163* (2), A251–A254
- (55) Tokur, M.; Algul, H.; Cetinkaya, T.; Uysal, M.; Akbulut, H. Improved Electrochemical Performance of Lithium Oxygen Batteries with N-Methyl-2-Pyrrolidone Based Composite Polymer Electrolytes. *J. Electrochem. Soc.* **2016**, *163* (7), A1326–A1335.
- (56) Zhang, W.; Zuo, P.; Chen, C.; Ma, Y.; Cheng, X.; Du, C.; Gao, Y.; Yin, G. Facile synthesis of binder-free reduced graphene oxide/silicon anode for high-performance lithium ion batteries. *J. Power Sources* **2016**, *312*, 216–222.